Star formation in the NGC 2024 molecular ridge

Claire J. Chandler[1]
National Radio Astronomy Observatory[2], P.O. Box O, Socorro, NM 87801

and

John E. Carlstrom[3]
Owens Valley Radio Observatory 105-24, California Institute of Technology, Pasadena, CA 91125

ABSTRACT

High-resolution images of the NGC 2024 molecular ridge in CS(2–1), CO(1–0), and 3 mm continuum emission have been obtained using the Owens Valley millimeter array. The data are used to determine the temperature and dynamics of the ridge, and to ascertain the evolutionary state of the embedded protostars FIR2–7. Dust continuum emission is detected from all six FIR sources, and masses of ~ 1 M$_{\odot}$ are implied assuming a dust temperature of 30 K and a dust opacity index $\beta = 1$. The sources are resolved, the majority of the emission probably arising in extended envelopes around the embedded protostars rather than circumstellar disks.

The CS(2–1) follows the ridge closely, but does not always coincide with the FIR sources. The largest discrepancy is for FIR5, the brightest of the dust continuum sources, where column densities derived from the dust and the CS differ by an order of magnitude. Although either depletion of CS or anomalous grain properties in FIR5 can explain this result, we also show that if the dust and gas temperature is $\gtrsim 100$ K for this compact source the two column density estimates may be brought into agreement.

The CO(1–0) traces the structure of the compact outflow from FIR6, and reveals a new outflow from FIR4. The latter is unipolar, with only a redshifted lobe, but is oriented symmetrically opposite the infrared reflection nebula associated with this source. Assuming the dynamical ages of the outflows from FIR4–6 are proportional to the age of the underlying

---

[1]Postal address: Mullard Radio Astronomy Observatory, Cavendish Laboratory, Madingley Road, Cambridge CB3 0HE, United Kingdom

[2]The National Radio Astronomy Observatory is a facility of the National Science Foundation operated under cooperative agreement by Associated Universities, Inc.

[3]Postal address: Department of Astronomy and Astrophysics, University of Chicago, 5640 S. Ellis Avenue, Chicago, IL 60637

protostars, an evolutionary sequence is suggested in the ridge. The formation of so many young protostars at locations separated by ~ 0.3 pc may have been triggered by the interaction of the NGC 2024 HII region with the molecular gas.

Subject headings: stars: formation - circumstellar matter - radio continuum: stars - interstellar medium: individual objects: NGC 2024

1. Introduction

The Orion Molecular Cloud complex offers the closest laboratory in which to study massive star formation. A particularly interesting region is NGC 2024, situated at a distance of 415 pc (Anthony-Twarog 1982), which harbors young stars at all stages of evolution. It includes a ridge of dense molecular material with a number of protostars showing signs of outflow activity (Sanders & Willner 1985; Richer 1990; Subrahmanyan 1992; Richer, Hills, & Padman 1992) coincident with an HII region approximately 1 parsec in extent. An infrared cluster has been identified toward the HII region (Barnes et al. 1989; Lada et al. 1991).

At optical wavelengths the appearance of the HII region is dominated by a dark dust lane located in front of the ionized gas. To the south the HII region is ionization-bounded by the dense molecular ridge, and exhibits considerable molecular hydrogen emission (Barnes et al. 1989). To the north the ionized gas expands away from the molecular cloud. The dust emission from the ridge has been mapped at 1.3 mm and 870 μm and found to contain seven compact sources, FIR 1–7, interpreted as isothermal protostellar condensations (Mezger et al. 1988; 1992). The ridge is believed to lie behind the HII region, and the high-resolution imaging of the HII emission by Gaume, Johnston, & Wilson (1992) indicates an interaction between the ionized gas and the dense molecular material.

The suggestion that the seven compact sources in the molecular ridge are isothermal condensations on their way to forming protostars has prompted detailed investigations into the nature of the dense cores (e.g., Moore et al. 1989; Schulz et al. 1991; Lis, Carlstrom, & Phillips 1991; Mauersberger et al. 1992; Graf et al. 1993; Wilson, Mehringer, & Dickel 1995). For several of the millimeter sources there now exists evidence that they contain embedded protostars or young stars: FIR4 is associated with a 2-μm source (Moore & Chandler 1989) and a reflection nebula (Moore & Yamashita 1995), FIR5 is the driving source of a highly collimated, unipolar, molecular outflow extending over several arcminutes (Sanders & Willner 1985; Richer et al. 1989; Richer et al. 1992), and FIR6 has a water maser (Genzel & Downes 1977) as well as a compact outflow with an extremely short dynamical age of ~ 400 yr (Richer 1990). The evolutionary states of FIR1–3 and FIR7 have yet to be determined.

Stars at all phases of evolution have been identified in NGC 2024: B stars ionizing the HII region, young stars that are members of the IR cluster, embedded protostars, and possibly some condensations that may yet form stars. It is therefore an ideal location in which to investigate the relationship between forming stars and their immediate surroundings, the interaction of HII regions and outflows with dense molecular gas, and the energy input and dissipation of molecular clouds by the star formation process. High spatial resolution is essential to reveal the structure of the individual FIR sources and their local environments, to determine whether hierarchical structure exists in the molecular cloud, and to find additional condensations and protostellar sources in the cloud not yet revealed by single-dish measurements. Interferometry is particularly important in this respect, as its spatial filtering properties reject the extended emission from the cloud and the HII region, allowing detailed imaging of compact objects and the high-velocity gas associated with the FIR sources (Barnes & Crutcher 1990; Wilson et al. 1995). Here we present a detailed interferometric study of NGC 2024 in CO J=1–0 and CS J=2–1, and in the continuum emission at 112.4 GHz and 98.0 GHz (2.67 mm and 3.06 mm). The main isotope of CO is selected for maximum brightness sensitivity to the high-velocity gas associated with the outflows; the higher dipole moment of the CS molecule makes it ideal for tracing gas with $n \gtrsim 10^5$ cm^{-3}. Our measurements reveal the relationship between the dense gas and the FIR continuum sources, and may suggest a temporal and spatial sequence to the star formation within the NGC 2024 molecular cloud.

2. Observations

The NGC 2024 observations were obtained with the 3-element millimeter array of the Owens Valley Radio Observatory (OVRO) between 1991 December and 1992 April. The CS(2–1) transition at 97.980968 GHz, and the CO(1–0) transition at 115.271204 GHz, were each observed using three separate pointing centers of the $\sim 1.1'$ FWHM primary beam to cover the dust ridge from FIR2 to FIR7. The positions of the pointing centers are listed in Table 1. The cryogenically cooled SIS mixer receivers gave typical single sideband (SSB) system temperatures, scaled to above the atmosphere, of 250 K for CS and 750 K for CO. The mixers could be tuned to reject the upper sideband (USB) by roughly 10:1, so the CS emission was observed in the lower sideband (LSB). The CO emission was observed in the USB with a sideband ratio of ~ 1, however, since the local oscillator system was designed to tune only to 115.5 GHz because of the strong atmospheric oxygen line at 118 GHz. The complex cross-correlations were performed using a single channel analog correlator with a 350 MHz bandwidth, and using a digital correlator for high spectral resolution. The digital spectrometer was set up to provide both a narrowband high-resolution configuration and a wideband low-resolution configuration for both transitions. This resulted in velocity resolutions of 0.38 and 3.06 km s^{-1} for the CS(2–1), and 1.30 and 5.20 km s^{-1} for the CO(1–0). The wideband channel (350 MHz) was used to measure the continuum emission at 112.4 GHz, the LSB frequency for the CO(1–0) observations.

The atmospheric and instrumental gain was monitored by observing the quasar 0529+075, and the bandpasses were measured using 3C273, 3C84, and 3C454.3. The absolute flux density calibration was determined from 3C273, 3C84, and 3C454.3, whose flux densities were bootstrapped from observations of Neptune and Uranus. The uncertainty in the flux density scale is estimated to be 10% at 98 GHz, and 15% at 112 and 115 GHz.

The data were edited and calibrated using software specific to the OVRO mm-array (Scoville et al. 1993), and were imaged and CLEANed using the AIPS reduction package. To remove contaminating continuum emission from the spectral line data, images made using the line-free channels of the low-resolution data were subtracted from the spectral line images. The data from each of the three pointings were corrected for the response of the primary beam, and then combined. The rms noise level is therefore not constant over the entire map. The boundaries of the combined images shown in this paper reflect the 50% response contour of the combined fields. Table 2 lists the uniformly-weighted synthesized beams as well as the conversion factors for converting flux densities to beam-averaged brightness temperatures, $T_{\rm B}$. Table 2 also lists the rms noise appropriate for the center of each field.

NGC 2024 lies close to the Celestial equator causing high sidelobes oriented north-south in the synthesized beam. Extended HII emission together with the north-south dust ridge therefore makes deconvolution of the point spread function difficult, especially for weak and/or extended features. A further complication for interferometric imaging of the NGC 2024 continuum emission is the presence of two bright features in the HII region (see, e.g., Gaume et al. 1992). These features are extended east-west, with one directly north of the other at a spacing similar to the sidelobes of the synthesized beam, causing negative features oriented east-west in our continuum images. Similar problems are evident in previous interferometric images of the continuum emission (Gaume et al. 1992; Wilson et al. 1995).

3. Results

3.1. Continuum emission

Continuum emission is detected from all of the six FIR sources covered by our three fields. Images of the continuum emission at both 98 and 112 GHz are shown in Figure 1, with crosses marking the positions of FIR2–6 from Mezger et al. (1988) and FIR7 from Mezger et al. (1992). At 98 GHz free-free emission from ionized gas in the HII region is clearly detected at the location of the Northern Compact Peak (NCP) east of FIR4, and the Southern Compact Peak (SCP) 20″ north of FIR5. Corresponding structures are also evident at 112 GHz, but the hole in the center of the *uv* plane is larger at the higher frequency, resulting in less sensitivity to the extended HII emission.

The 98 and 112 GHz continuum images can be used to obtain an estimate of the spectral index, α, for the compact sources. With only 14% difference in frequency between the two measurements, the spectral index is not very well constrained. Furthermore, the difference in *uv* coverage between the 98 and 112 GHz maps may cause an underestimate of α, since more of the emission will be resolved out at 112 GHz. Nevertheless the interpretation of the spectral index derived from these two interferometric images is more straightforward than interpreting the spectral index obtained using interferometric flux density measurements at 3 mm and the 1.3 mm single-dish data of Mezger et al. (1988), since much of the extended emission is resolved out by the interferometer. This may explain why the spectral indices for the FIR sources derived from 3 mm BIMA measurements and the 1.3 mm single-dish data by Wilson et al. (1995) are all in the range 4–5.

The spectral indices were obtained as follows: first the 98 and 112 GHz continuum images were each restored with the same CLEAN beam. Regions were blanked in both images if the intensity was less than the mean rms noise in either image. For each source the integrated flux densities in the blanked images were then used to calculate the spectral index. Table 3 lists the resulting spectral indices for all FIR sources and both HII continuum peaks. The values of α for both the NCP and SCP are, within the errors, consistent with a free-free spectral index of -0.1. All FIR sources apart from FIR4 have a positive spectral index, although the closeness in frequency between the two continuum measurements results in large uncertainties in the derived value of α, and the spectral indices for FIR6 and FIR7 are also consistent with $\alpha < 0$. For optically-thin dust emission in the Rayleigh-Jeans regime $\alpha = 2 + \beta$, where β is the power-law frequency dependence of the dust opacity, $\kappa_\nu \propto \nu^\beta$. The emission from FIR2, FIR3, FIR5, FIR6 and FIR7 is thus entirely consistent with originating from dust with β in the range 0–2, while FIR4 may require an extra component with a flatter spectrum.

Positions and flux densities integrated over a 10″ box centered on each FIR source are also listed in Table 3. Masses have been derived from the 3 mm flux densities, F_ν, by assuming that all the emission arises from dust and that the emission is optically thin, using

$$M = \left(\frac{F_\nu D^2}{\kappa_\nu B_\nu(T)}\right), \quad (1)$$

or

$$\frac{M}{M_\odot} = 3.2 \times 10^{-11} \left(\frac{F_\nu}{\mathrm{mJy}}\right) \left(\frac{D}{\mathrm{pc}}\right)^2 \left(\frac{\kappa_{10^{12}\ \mathrm{Hz}}}{0.1\ \mathrm{cm}^2\ \mathrm{g}^{-1}}\right)^{-1} \left(\frac{\nu}{10^{12}\ \mathrm{Hz}}\right)^{-(3+\beta)} \left(e^{h\nu/kT} - 1\right). \quad (2)$$

In equation 2 above we have adopted a value $\kappa_\nu = 0.1(\nu/10^{12}\mathrm{Hz})^\beta)$ cm^2 g^{-1} for the dust mass opacity coefficient (cf. Hildebrand 1983; Beckwith et al. 1990), but note that it is fairly uncertain, particularly for the dense condensations observed here. For a dust temperature of 30 K, similar to the temperature obtained from molecular line studies of the dense cores (e.g., Chandler, Moore, & Emerson 1992; Ho et al. 1993), $D = 415$ pc, and $\beta = 1$, the mass traced by the 3 mm dust emission is of order 1 $M_\odot$ for all the FIR sources. For the above dust parameters our 1σ detection level corresponds to 0.04 $M_\odot$ beam^{-1}.

3.1.1. Individual continuum sources

The only point-like source detected at 3 mm is IRS2, an early B star located within the HII region at the 50% sensitivity level in the 98 GHz image to the east of FIR3. All the other detected sources are extended. Emission from FIR2 is observed at both 98 and 112 GHz, but the peak is offset by about 5″ in the two images. The source is extended and does not have significant compact structure. As the 1.3 mm continuum map of Mezger et al. (1988) demonstrates, there is considerable extended emission from the dust ridge around FIR2 and FIR3, and the appearance of both sources are probably sensitive to the precise *uv* coverage of the interferometer data. FIR3 is resolved at both frequencies, with an average source size of $\approx 4''$ derived from fitting Gaussians to the two continuum images. Inspection of Figure 1 shows that the orientation of FIR3 differs by $\sim 90°$ from one frequency to the other, and demonstrates the imaging problems caused by the combination of extended source structure and the poor coverage of the *uv* plane at the Celestial equator. Source sizes derived from these data are therefore only approximate.

The emission from FIR4 is confused with that from the NCP, which may account for the low value of α in this source (Table 3). At 98 GHz there is a clear peak close to the 1.3 mm position for FIR4, and a comparison with the 1.3 cm continuum image of Gaume et al. (1992) shows there is no counterpart from ionized gas at this location. We therefore identify this source with FIR4. The compact peak in the NCP 25″ to the east of FIR4 coincides with the peak in the NCP emission observed by Gaume et al.

At the higher resolution of the 112.4 GHz continuum image, FIR5 comprises a compact source of $\approx 2''$ FWHM, plus an extension to the east. The orientation of the extension is perpendicular to the large-scale outflow. The extended emission associated with FIR5 may indicate the presence of companion protostars. Studies of similar objects in more nearby star forming regions indicate that multiple sources may be common, but they are only evident when high spatial resolution data become available (e.g., IRAS 16293 in ρ Ophiuchus: Mundy et al. 1992, Walker et al. 1993; IRAS 4 in NGC1333: Lay, Carlstrom, & Hills 1995). The frequency of binaries or multiple sources in early phases of protostellar evolution is not yet known due to the lack of high resolution, high sensitivity observations.

FIR6 also shows a $2''$ compact source and emission extended to the north-east, toward the blueshifted lobe of its compact outflow (Richer 1990; see § 3.2.4). To investigate whether any 1.3 cm continuum emission is associated directly with the FIR sources, we inspected the VLA data presented by Gaume et al. (1992; R. Gaume, private communication). The data clearly exhibited the problems associated with interferometric imaging of the NCP and SCP in the presence of extended emission from the HII region, with positive and negative ripples oriented east-west. To try to minimize these problems a number of images were made by Gaume after removing the short *uv* spacings. The only 1.3 cm (23.7 GHz) emission detected in these maps that appears to be associated with the FIR sources is a small feature displaced $2''$ east of the position for the peak millimeter intensity toward FIR6 (Table 3). The integrated flux density of this feature is 21 ± 6 mJy; the peak of 10 mJy is detected at the 7σ level. Both the magnitude of the 1.3 cm flux density and the fact that the emission is coincident with the high-velocity blueshifted CO suggest that the centimeter emission from FIR6 may originate in an ionized wind or jet. Assuming a spherical wind with a velocity of 100 km s^{-1}, the 1.3 cm flux density corresponds to a mass-loss rate of 5×10^{-7} M$_\odot$ yr^{-1} (Panagia & Felli 1975). However, if the ionized gas is collimated, as is highly likely, the mass-loss rate required to produce the radio emission may be considerably lower (Reynolds 1986).

3.2. Molecular line emission

3.2.1. CS(2–1)

As has been noted in a number of high-resolution studies, the dense gas in NGC 2024 is located close to, but not always coincident with, the dust continuum sources in the ridge (e.g., Mauersberger et al. 1992; Wilson et al. 1995). This phenomenon is demonstrated in Figure 2, where the CS(2–1) emission from the ridge integrated from $V_{\rm LSR} = 1.8$ to 20.2 km s^{-1} is shown, with the positions of the FIR sources from Table

2 marked as stars. There is evidence for missing flux due to extended emission in the ridge, resulting in negative features in the image. Comparing the integrated flux shown in Figure 2 with the CS(2–1) observations of Snell et al. (1984) indicates that $\sim 35\%$ of the total flux density in the primary beam has been detected by the interferometer.

The CS(2–1) emission is located in two main complexes: a ring of emission to the north and east of FIR5 and FIR6, and a ridge between FIR2 and FIR3. Filamentary structures are observed in the central field, which also have counterparts in the $11''$ resolution CS(5–4) maps of Schulz et al. (1991). The peak values of the beam-averaged brightness temperature, $T_{\rm B}$, from the narrow-band channel data for the main complexes are 44 K for FIR5/FIR6 close to the SCP, and 35 K for the FIR2/FIR3 ridge.

Six distinct condensations are apparent in the CS complex at FIR5/FIR6: three aligned along the axis connecting FIR5 and FIR6, and three in a parallel line offset $12''$ to the east. Together these six condensations form a ring, and the CS(2–1) is probably tracing the same structures identified in the lower resolution HCO^+(1–0) observations of Barnes & Crutcher (1990). A spectrum obtained toward each condensation is presented in Figure 3. Toward condensations 2, 3 and 4 in the north of the complex, the line profile is approximately Gaussian and single-peaked, while toward the southern condensations 1 and 6 the outflow from FIR6 is visible as high-velocity wing emission, mainly blueshifted, extending ≈ 10 km s^{-1} away from the cloud velocity. The southern condensations 1, 5 and 6 also show dips in their spectra at 11.2 km s^{-1}, which is the velocity of the cloud at this position (e.g., Schulz et al. 1991; Mauersberger et al. 1992). Since the CS(2–1) line is optically thick and extended the dip in the spectra is probably due to the interferometer resolving out a large fraction of the CS(2–1) emission at those velocities. Consequently the mass derived toward FIR6 from the CS(2–1) emission is underestimated.

In order to calculate the mass of the gas traced by the CS(2–1) emission we use an abundance for CS relative to H_2 of 2.5×10^{-9} as found for the Orion ridge (Blake et al. 1987). The observed maximum brightness temperature provides a lower limit to the excitation temperature, so we assume $T_{\rm ex} = 40$ K. This value is very similar to the kinetic temperature derived from LVG modeling of the CS(7–6) and 5–4 lines by Schulz et al. (1991), who find that $T_{\rm kin}$ lies in the range 35–40 K for the various single-dish CS peaks in the ridge. Schulz et al. also derive optical depths from their models for the 5–4 transition, τ_{54}, which lie in the range 5–8. In LTE with $T_{\rm ex} = 40$ K the optical depth ratio $\tau_{54}/\tau_{21} = 5.9$, so we assume a moderate optical depth of $\tau_{21} = 1$ in our calculations. We also assume LTE. The mass derived for the FIR5/FIR6 CS complex is then 12 $M_\odot$, the ridge around FIR7 is 1 $M_\odot$, the FIR2/FIR3 complex is 6 $M_\odot$, and the center field including FIR4 is 9 $M_\odot$. A total of 28 $M_\odot$ is therefore traced by the CS(2–1), which is approximately 20% of the total mass of the ridge traced by $C^{18}O$ (Mauersberger et al. 1992) and higher transitions of CS (Schulz et al. 1991).

Masses can also be derived from the virial theorem using the measured sizes and linewidths. The linewidths of the northern condensations in the FIR5/FIR6 complex are ~ 1.2 km s^{-1}, corresponding to a virial mass of 1.8 M$_\odot$ for an average clump size of $\sim 6''$. The mass derived from the CS(2–1) emission for each clump is in the range 1.1–2.4 M$_\odot$, indicating that the assumptions made about the CS(2–1) excitation above are reasonable for these condensations. Toward FIR6, however, the linewidth becomes dominated by the outflow, which is discussed further below.

Considerable velocity structure in the dense gas is revealed by the high spectral-resolution data. Figure 4 presents a first moment map of the CS(2–1) emission, in which the intensity at each position represents the flux weighted average velocity. Single dish measurements have revealed an overall velocity gradient along the ridge, with the northern field blueshifted relative to the southern field (Moore et al. 1989; Lis et al. 1991; Schulz et al. 1991). This trend is also detected here, with a mean $V_{\rm LSR}$ of 10.5 km s^{-1} in the north, and 11.1 km s^{-1} in the south. Within this general trend, however, there is an additional velocity gradient perpendicular to the long axis of the ridge, especially within the FIR5/FIR6 complex where the bar aligned with the FIR sources is redshifted by approximately 1.5 km s^{-1} relative to the CS condensations to the north and east.

The 1.5 km s^{-1} velocity gradient across the FIR5/FIR6 CS complex is consistent with that required for rotational support of the 12 M$_\odot$ core. However, perhaps the FIR6 molecular outflow (§ 3.2.4) is partly responsible for the gradient. The total kinetic energy deposited in the cloud by this outflow is 1.2×10^{45} ergs which, if evenly distributed in the 12 M$_\odot$ FIR5/FIR6 complex, would result in a velocity FWHM of 4.3 km s^{-1} over the whole region. This is clearly much larger than the velocity widths observed in the northern clumps, and is also larger than total velocity difference from one side of the core to the other. While the outflow energetics are certainly powerful enough to account for the gentle velocity gradient, most of its influence is clearly confined to the region around FIR6. The dynamics of the complex may also be influenced by shocks from the nearby HII region. The SCP is at a projected distance of only ~ 0.03 pc which leads to a crossing time of 3×10^4 yr at 1 km s^{-1}.

3.2.2. Comparison of CS(2–1) with the dust continuum

With the assumptions about the CS(2–1) excitation described above the 1σ mass sensitivity level in the integrated CS(2–1) map is 0.014 M$_\odot$, approximately a factor of 3 better than the dust emission. We can therefore compare directly the mass traced by dust with that traced by the CS(2–1) emission, bearing in mind the assumptions that have been made about the dust temperature, and the dust opacity. Figure 5 shows contours of the beam-averaged column density of hydrogen molecules, $N(\rm H_2)$, in steps of 7.4×10^{22} cm^{-2}; the heavy contours are derived from the CS(2–1) emission, and the lighter contours are from the dust emission. For FIR2, FIR3, FIR4, and FIR6, the column densities derived from the CS(2–1) and the dust are within a factor of two. However, the two methods of measuring the column density are highly discrepant toward FIR5 and the CS(2–1) clumps around FIR5/FIR6.

The lack of CS(2–1) emission toward FIR5 could be attributed to depletion of CS onto cold dust grains. Large depletion factors are expected for cold dense sources where depletion timescales are on the order of 10^3 yr, and molecular abundances roughly a factor of 10 lower than typical have been observed toward several embedded young stellar sources (e.g., Blake et al. 1995). While this provides a plausible explanation for the discrepancies between the column densities derived for FIR5 based on the CS(2–1) and the dust continuum emission, there are other possibilities which should also be considered. In particular, effects due to variations in the dust mass opacity coefficient as well as the dust temperature and gas excitation temperature could cause the apparent discrepancies.

Consider the dust mass opacity coefficient. If our adopted value at 3 mm is too low, either because the assumed value of β is too high, or because the normalization is inappropriate for grains in this environment, then the column density derived from the dust emission toward FIR5 would be overestimated. A value of $\beta = 1$ was used to calculate the dust mass, but our measurements indicate that $\beta = 1.6 \pm 1.4$ for FIR5. If β is at the high end of this allowed range the discrepancy is further exacerabated. Even if β is as low as 0.2, the peak column density then derived from the dust, $N(H_2) = 1.1 \times 10^{23}$ cm^{-2}, should have been detected easily in CS(2–1) emission. Thus if the discrepancy at FIR5 is caused by anomalous dust properties it is most likely that the normalization we have used is too low. We note, however, that for the CS clumps east of FIR5 a change from $\beta = 1$ to $\beta = 2$ would increase the calculated dust mass by a factor of 10, and would easily account for differences between the column densities derived by both methods apparent in Figure 5.

Alternatively, the discrepancies in the column density determinations toward FIR5 may indicate that the dust and gas temperatures are higher than the 30–40 K assumed in the calculations, since the line and dust emission have different temperature dependencies. The CS(2–1) optical depth is proportional to $N(H_2)/T_{ex}^2$ for $T_{ex} \gg 5$ K, while the dust optical depth is proportional to $N(H_2)$. The gas space density for FIR5 estimated from the dust emission is approximately 10^9 cm^{-3} for a source size of $\sim 2''$. It is expected that the CS excitation temperature and the dust temperatures should be well coupled at these high densities. In this case the ratio of the dust emission to the CS(2–1) emission will increase with the square of the temperature if the CS is optically thin, and will be independent of temperature [but proportional to $N(H_2)$] if the CS is optically thick. If the center of the CS(2–1) line is optically thick, while the line wings are thin, the dust/CS emission ratio will increase with both the temperature and the column density. Thus if the temperature of FIR5 is actually a factor of 3 or so higher than assumed above (i.e., > 100 K) and its CS emission is optically thin, then the column densities based on the CS(2–1) emission and the dust emission can be brought into agreement without invoking significant depletion of CS or anomalous grain properties. Such elevated temperatures were also suggested by Mauersberger et al. (1992) to explain discrepancies between the dust and $C^{18}O$ emission in the ridge, but were discounted on the basis of the low submillimeter color temperatures ($\sim$ 20 K) derived for the dust by Mezger et al. (1992). However, we show in § 4.1 that such low temperatures are not consistent with our interferometer data, and that the combination of high dust optical depths and temperature gradients in the dense cores can produce artificially low color temperatures.

A dust temperature of 100 K for a source size of $2''$ leads to a luminosity of 700 $L_\odot$. An independent estimate of the luminosity can be obtained from the mechanical luminosity of the FIR5 outflow and the empirical scaling relationships of outflow to source bolometric luminosities provided by Cabrit and Bertout (1992). The outflow mechanical luminosity of ~ 2 $L_\odot$ (Sanders & Willner 1985, Richer et al. 1989) indicates a source luminosity of ~ 200 $L_\odot$. Considering the large uncertainties in source size, the outflow properties and the scaling relationships, there is some support for a source luminosity of a few hundred $L_\odot$, and therefore high dust temperatures. Interferometric observations of high excitation transitions are needed to confirm such elevated gas temperatures.

Optical depth effects could also contribute to the discrepancies in the column densities derived from the gas and dust continuum emission. The apparent spatial extension of the continuum emission may be due to two or more extremely compact dust sources, such as accretion disks. The high optical depth of the CS(2–1) emission from such objects, and the small beam filling factors, would drastically reduce the column density sensitivity of our CS observations. Such disks would be unusually massive, however. Interferometric dust continuum observations with $\lesssim 1''$ resolution are necessary to probe further the compact structure of FIR5.

If the discrepancies in the column density determinations are caused by assuming too low temperatures or too low CS(2–1) optical depths toward unresolved compact distributions, we must still ask why there is apparently no envelope of cooler gas that would emit strongly in CS(2–1). One possible explanation is that the source is sufficiently evolved that its outflow has already dispersed the lower density extended material.

3.2.3. CO(1–0)

In Figure 6 we show channel maps of the ^{12}CO J=1–0 emission from NGC 2024 observed with 5.2 km s^{-1} resolution. The CO emission close to the cloud velocity of 11 km s^{-1} is optically thick and extended, and Figure 6 shows imaging problems due to missing flux in the 8.4 and 13.6 km s^{-1} channels. An image was made of the CO emission integrated from $V_{\rm LSR} = -31$ km s^{-1} to $+53$ km s^{-1}; no emission was detected outside this velocity range. The image quality is poor due to the missing flux; comparison with the single-dish data presented by Sanders & Willner (1985) shows that less than 30% of the total flux density in the CO(1–0) line is recovered by the interferometer.

Emission from the compact outflow at FIR6 dominates the channel maps at blueshifted velocities. At redshifted velocities the red counterpart to the FIR6 flow is detected, as is emission from the large-scale outflow from FIR5. Features at velocities from 14 to 29 km s^{-1} located south of FIR5 and west of FIR6 correspond to structures observed in the CO(2–1) line by Richer et al. (1992).

The peak beam-averaged brightness temperature detected in the high-velocity gas from FIR6 is 37 K, and for the FIR4 outflow (see below) the peak $T_{\rm B}$ is 50 K. These are somewhat higher than the value of 25 K used by Richer (1990) for FIR6, and his values for the mass, momentum, and energy of that outflow should be revised up by a factor of 1.4 if the excitation temperature for FIR6 is also closer to 50 K. To determine whether the high-velocity emission is optically thick we compared the integrated CO(1–0) flux density in the blue and red lobes of FIR6 with that observed in CO(2–1) by Richer. In LTE with $T_{\rm ex}$ = 50 K the ratio of the optical depths in the two lines is $\tau_{21}/\tau_{10} = 3.4$. The flux density ratio in the optically-thin limit is therefore $S_{21}/S_{10} = 12.9$. In the blue lobe of the outflow $S_{21}/S_{10} \approx 7$, giving lower limits to the optical depth in each transition of $\tau_{10} \gtrsim 0.6$, and $\tau_{21} \gtrsim 2$. We therefore confirm the validity of the assumption made by Richer (1990) that the J=2–1 emission is optically thick in FIR6. In the red lobe we observe $S_{21}/S_{10} \approx 35$, indicating that only 35% or less of the redshifted J=1–0 emission is detected by the interferometer.

3.2.4. Outflow from FIR6

The high-velocity CO(1–0) and CS(2–1) emission in the vicinity of FIR6 is shown in Figure 7, overlaid on a greyscale image of the integrated CS(2–1) emission tracing the dense gas in the NGC 2024 ridge. The CO(1–0) is integrated over the velocity ranges $|V - V_{\rm LSR}|$ = 10 to 42 km s^{-1}, and the ranges for the CS(2–1) are $|V - V_{\rm LSR}|$ = 2.10 to 7.84 km s^{-1}. The correspondence of the blueshifted lobe traced by the CO(1–0) and the CS(2–1) is extremely good, and the bipolar nature of the outflow is evident in both molecular lines. The symmetry of the blue- and redshifted lobes, especially in CS(2–1) emission, supports the identification of FIR6 as the origin of the outflow, rather than the suggestion of Chernin (1996) that the flow is being driven by an as-yet undetected, low-mass source.

The structure of the outflow as traced by the CO(1–0) emission is in good agreement with that observed in the J=2–1 line by Richer (1990). With the higher spatial resolution provided by interferometry, however, it is seen that the position angle of the blue lobe changes as a function of velocity (Figure 6). At 3 and -2 km s^{-1} the outflow has the same $\sim 30°$ position angle as the low-level contours in our 98 and 112 GHz continuum maps. At more extreme blueshifted velocities the position angle is closer to 75°. The different position angles may indicate variability in the direction of the driving wind or jet, or an interaction with ambient cloud material. Since most of the dense gas is located to the north of FIR6 (see Figure 2), we argue below that the structure of the FIR6 outflow is primarily determined by the interaction of a wind from FIR6 with nearby dense clumps in the ridge.

The mass and momentum of the outflow traced by the CS(2–1) is approximately a factor of three higher than that observed in the high-velocity component of the flow ($|V - V_{\rm LSR}| \approx 10$ to 70 km s^{-1}) by Richer (1990) in CO(2–1) emission. Assuming an excitation temperature of 40 K and $\tau \ll 1$ in the line wing, the mass of the blue lobe derived from the CS emission is 0.58 M$_\odot$, and the red lobe is 0.20 M$_\odot$. The momentum of each lobe is 4.5 M$_\odot$ km s^{-1} (blue) and 1.6 M$_\odot$ km s^{-1} (red). These compare with a total mass and momentum derived from the CO emission of 0.13 M$_\odot$ and 2.1 M$_\odot$ km s^{-1} in the high-velocity component. The energy of the flow from the CS(2–1) emission is comparable with that derived from the high-velocity CO emission, but the mechanical luminosity is considerably lower. The energy is 5×10^{44} ergs from CS, compared with 7×10^{44} in the CO, and the mechanical luminosity is only 1.2 L$_\odot$ in the CS compared with 15 L$_\odot$ in the CO. The difference in the luminosity is mainly due to the longer dynamical timescale derived from the CS emission (3300 yr compared with 400 yr from the CO), since no CS emission is detected at velocities larger than 8 km s^{-1} away from the systemic velocity of the cloud.

The position angle of the CS outflow agrees well with the high-velocity CO emission; both appear to be tracing the component of the flow with the highest momentum. At low velocities the CO(1–0) emission is extended to the north-east, in the direction of the dense gas. The outflow gas in FIR6 is concentrated in compact clumps, similar to the FIR5 flow (§ 3.2.5), and enhanced CO(1–0) emission is located at the edges of the CS condensations closest to FIR6. The velocity width of these CO clumps is non-thermal, in some cases as high as 5 km s^{-1}, and must be attributed to the local interaction of the driving wind with molecular gas in a shock, or by hydrodynamic instabilities in the flow as has been suggested for the outflow from FIR5 (Richer et al. 1992). Given the coincidence of the enhanced CO emission with the CS condensations, it is most likely that the CO(1–0) clumps in the outflow are sites of temperature or density enhancements in shocks, where the driving wind is impinging on the nearby dense gas.

3.2.5. Outflow from FIR5

The interferometer measurements show that the CO(2–1) intensity peaks observed by Richer et al. (1992) break up into smaller clumps approximately $4''$ ($\sim$ 1700 AU) in size. At 19 km s^{-1} the outflow appears to have a limb-brightened, shell-like structure, and the emission at 24 km s^{-1} is located inside this shell and is more collimated. Since the outflow does not align directly with FIR5, Chernin (1996) argues that its origin must not be FIR5, but a lower-luminosity object not detected at millimeter wavelengths. This seems unlikely given the large mechanical luminosity of the outflow (~ 2 L$_{\odot}$: see Richer et al. 1992). The high-resolution CS(2–1) data presented here suggest instead that the misalignment may be explained by the location of a sharp density gradient in the cloud to the south and east of FIR5. As Richer et al. point out, the flow is probably following the path of least resistance.

3.2.6. Outflow from FIR4

A unipolar, redshifted outflow from FIR4 is also detected by our CO(1–0) measurements. It extends to the southeast of FIR4, and is located directly opposite the infrared reflection nebula imaged by Moore & Chandler (1989) and Moore & Yamashita (1995). In Figure 8 the CO emission from FIR4 integrated between 13.5 and 20 km s^{-1} is shown overlaid on the 2-μm continuum emission. The alignment of the high-velocity gas opposite the reflection nebulosity is consistent with the blueshifted lobe of a bipolar outflow from FIR4 having broken through the back face of the foreground HII region, while the redshifted lobe extends back into the molecular cloud.

The spatial extent of the FIR4 outflow is $\approx 13''$, and the maximum extent in velocity is ≈ 10 km s^{-1}, giving a dynamical timescale L/V of 2600 years. Assuming an excitation temperature of 50 K, $\tau = 1$, and a CO abundance relative to H_2 of 1×10^{-4} we find values for the mass, momentum, energy, and mechanical luminosity of the redshifted lobe of FIR4 of $M = 0.04$ M$_{\odot}$, $P = 0.4$ M$_{\odot}$ km s^{-1}, $E = 4 \times 10^{43}$ ergs, and $L_{\rm CO} = 0.13$ L$_{\odot}$ respectively. No correction has been made for inclination, and since the blueshifted counterpart has no molecular gas with which to interact, the momentum and energy of the flow may be a factor of ~ 2 higher. Comparing these values with those derived for FIR5 and FIR6 (Richer et al. 1992; Richer 1990), FIR4 is clearly the weakest of the three outflow sources in the NGC 2024 ridge.

4. Discussion

4.1. Evolutionary state of the FIR sources

The age and evolutionary state of the FIR sources in the NGC 2024 ridge has been under debate ever since Mezger et al. (1988, 1992) suggested they may be protostellar condensations, based on their low dust color temperatures derived from 1.3 mm and 350 μm continuum emission, and assuming $\beta = 2$. Although there is considerable far-infrared emission from the ridge, and evidence for dust and gas with temperatures in excess of 40 K, Mezger et al. argued that this warmer component was extended and heated by the HII region and was unrelated to the FIR condensations, which had temperatures closer to 15–20 K. With the high spatial resolution afforded by millimeter interferometry we are now able to make measurements to test this hypothesis directly.

The beam-averaged brightness temperature of the dust emission for each source at both 98 and 112 GHz, $T_{\rm 3mm}$, is listed in Table 4. If the true dust temperature is $T_{\rm d}$, then the optical depth of the millimeter emission is $T_{\rm 3mm}/T_{\rm d}$ and the corresponding optical depth at 350 μm is then $(T_{\rm 3mm}/T_{\rm d})(\lambda_{\rm 3mm}/350\mu{\rm m})^{\beta}$. The value of $\tau_{350\mu{\rm m}}$ is listed in Table 4 for the FIR sources, assuming $\beta = 2$ and $T_{\rm d} = 20$ K. Note that these values are lower limits, since the interferometer resolves out some of the flux. For all sources apart from FIR7 a dust temperature as low as 20 K implies that the 350 μm emission has a considerably higher optical depth than that derived by Mezger et al. (1988), and calls into question the derivation of a color temperature using only the 350 μm and 1.3 mm emission. Specifically, the dust temperature may be underestimated if there is a temperature gradient in the cloud, for example, due to the presence of an embedded heat sources. Under these circumstances optically-thick 350 μm emission will arise at a radius where the dust is cooler than in the center, and the mm-wavelength emission may be enhanced relative to the submm by a large factor. We therefore argue that for most of the FIR sources the low temperatures Mezger et al. derived from the 1.3 mm and submm emission assuming $\beta = 2$ are not consistent with the high-resolution interferometer data presented here.

The association of FIR4, FIR5, and FIR6 with energetic outflows shows that these sources already harbor protostars or young stellar objects. The FIR5 flow appears to be the most evolved of the outflows in NGC 2024, with a highly-collimated redshifted jet extending over $\sim 5'$ (Richer et al. 1992). FIR5 itself is close in projection to the SCP in the HII region, and it has been suggested that the lack of a distinct blueshifted counterpart to the extended redshifted CO outflow is due to the fact that the flow emerges into the HII region and is photodissociated (Richer et al. 1992). Some support is given to this idea by the 330 MHz continuum data presented by Subrahmanyan (1992), which shows a jet-like extension of the ionized gas north of the large-scale HII region extending a total of $11'$ (1.3 parsecs) from FIR5. Subrahmanyan also detects a counter jet coincident with the redshifted FIR5 flow, which may be shock-heated gas entrained in the molecular jet.

A 2-μm source extended east-west has been detected from FIR4 (Moore & Yamashita 1995), indicating that its outflow has disrupted the surrounding envelope sufficiently to make either the driving source or nebulosity close to the source visible through the back face of the HII region. FIR4 lies close to the NCP, which has been interpreted by Gaume et al. (1992) as the location where the molecular ridge protrudes into the HII region. The mm continuum emission from FIR4 is extended over approximately $7''$ and may trace the location of warm dust heated either by the outflow or the HII region, in addition to any weak compact dust component.

The compact outflow from FIR6 has one of the shortest dynamical timescales yet measured (400 yr: Richer 1990). Its appearance is dominated by the interaction with the nearby dense gas to the north of FIR6 rather than the HII region, unlike FIR4 and FIR5. Assuming that outflows begin at a fixed time in the evolution of protostars, the compact flows from FIR6 and FIR4 suggest that these sources are younger than FIR5.

Both FIR5 and FIR6 display compact dust components in our mm continuum images. Compact dust emission has been observed around a number of young protostars, and often can be divided into contributions from an unresolved disk component and an extended envelope (e.g., Ohashi et al. 1991; Terebey, Chandler, & André 1993; Hayashi, Ohashi, & Miyama 1993; Lay et al. 1994; Chandler et al. 1995; Lay et al. 1995). The fraction of circumstellar material in a disk relative to the envelope is expected to increase with age; the fact that we observe masses for FIR5 and FIR6 considerably larger than any yet observed for a disk around a young star indicates that we are most likely detecting their extended envelopes. This is also supported by the fact that we resolve the dust emission. With so much mass still remaining in the envelope both sources are probably very young.

Of the remaining sources FIR3 is the only one that shows compact emission. However, no other sign of star formation (such as high-velocity gas or a near-infrared source) has yet been associated with it. Neither FIR2 and FIR7 show compact emission, and FIR7 has the lowest brightness temperature of all six sources in the ridge. These objects may be closer to the isothermal condensations originally proposed by Mezger et al. (1988). The CS(2–1) condensations around FIR5/FIR6 are also massive enough to form stars, and could also represent a very early phase of star formation.

4.2. Sequential star formation in NGC 2024?

Dividing the length of the ridge, ~ 0.3 pc, by the observed linewidths, ~ 1 km s^{-1}, gives a crossing time of $\sim 3 \times 10^5$ yr. If we assume that the dynamical timescales of the outflows are proportional to their ages, then FIR5 ($t_{\rm dyn} \sim 1.4 \times 10^4$ yr) is the oldest and also has the largest outflow. FIR4 ($t_{\rm dyn} \sim 2.6 \times 10^3$ yr) and FIR6 ($t_{\rm dyn} \sim$ 400–3300 yr) are younger and have much more compact outflows. The other objects, FIR2, FIR3, FIR7, and the CS condensations, are all less luminous, and probably younger than the outflow sources. Note that these ages are all much less than the crossing time and even though the dynamical times most likely underestimate the age of outflows (e.g., Parker, Padman, & Scott 1991), it suggests that a central or external trigger has synchronized the star formation over the length of the ridge. The expansion of the HII region into the cloud is the obvious choice for the trigger. This is further supported by the observation that the ages of the protostars in the NGC 2024 molecular ridge seem to decrease with their distance from the NCP or the SCP, the locations of strong interaction between the HII region and the dust ridge.

5. Conclusions

High angular resolution interferometric observations in continuum emission and in CS(2–1) and CO(1–0) have been used to determine the physical conditions within the NGC 2024 ridge, and the evolutionary state of the embedded protostars, FIR2–7. From the 98 GHz and 112 GHz continuum we obtain spectral indices for FIR2, FIR3, FIR5, FIR6 and FIR7 consistent with dust emission; for FIR4 an extra component is required with a shallower spectral index, presumably free-free emission. The CS(2–1), which traces gas with $n \gtrsim 10^5$ cm^{-3}, follows the ridge closely, but does not always coincide with FIR sources. The largest discrepancy occurs for FIR5, where the column densities derived from the dust emission and from the CS(2–1) differ by an order of magnitude. Although depletion of CS in the dense core or anomalous grain properties can explain this result, we show that an increase in both the dust temperature and the CS(2–1) excitation temperature to $\gtrsim 100$ K can bring the two column density estimates into agreement. Such a high temperature results in a much larger luminosity for FIR5 than previously implied by the low dust temperatures proposed by Mezger et al. (1988; 1992), but is consistent with the association of an energetic outflow with FIR5. The column densities based on the CS and dust emission agree to within a factor of 2 for the other FIR sources if a dust opacity with $\beta = 1$ and $T_{\rm d} = 30$ K is assumed. However, there are locations where considerable CS(2–1) emission is detected with beam-averaged brightness temperatures of ~ 40 K, and with no corresponding continuum emission. At these locations a dust opacity with $\beta = 2$ brings the two column density estimates into agreement, suggesting that the properties of the dust in the ridge may be different from the FIR sources.

The CO(1–0) data trace the compact outflow structure of FIR6, and show that emission from the high-velocity gas in both the FIR6 and FIR5 outflows breaks up into clumps with sizes of $\sim 4''$. The clumps in the FIR6 flow have velocity widths of ~ 5 km s^{-1}, which probably reflect an interaction of the driving wind with the ambient cloud. The FIR6 outflow is also apparent in the CS(2–1) images, where it is highly collimated. Most of the momentum in the outflow is in the low-velocity material traced by the CS emission.

The CO(1–0) data have also revealed a new compact outflow associated with FIR4. This new outflow shows only redshifted emission, but it is located symmetrically opposite the near-infrared reflection nebula reported by Moore & Yamashita (1995).

If the dynamical ages and extents of the outflows from FIR4–6 are taken to be indicative of the age of the underlying protostar, an evolutionary sequence is suggested in the ridge. FIR5 is the oldest and has the largest, most evolved outflow; FIR4 and FIR6 are younger and have small, compact outflows. The remaining FIR sources and CS condensations do not yet show signs of star formation. FIR4 and FIR5 are very close in projection to the NCP and SCP, which are free-free emission peaks thought to arise where the ridge protrudes into the HII region. An interaction of the HII region with the molecular gas, triggering the formation of the FIR sources, provides a natural explanation for so many protostars in similarly early phases of evolution being distributed over ~ 0.3 pc along the ridge.

We are grateful to John Richer for his careful reading of the paper, and for comments which have improved the clarity of the text. We thank Ralph Gaume for allowing us to use his 1.3 cm data, and Toby Moore for providing the 2-μm image in Figure 8. JC gratefully acknowledges support from a NSF-YI award and the David and Lucile Packard Foundation. Research at the Owens Valley Radio Observatory is supported by NSF grant AST 93-14079.

Table 1. Pointing centers for NGC 2024 fields.

Field	R.A. (1950) (h m s)	Dec. (1950) (° ′ ″)
North	05 39 11.50	−01 55 47.0
Center	05 39 12.70	−01 56 37.0
South	05 39 13.70	−01 57 27.0

Table 2. Imaging parameters for the 3 mm observations of NGC 2024.

Transition	Synthesized beam (″)	Bandwidth (MHz)	Bandwidth (km s^{-1})	Rms noise per field (mJy)	Mean rms over ridge[a]	K/Jy
98.0 GHz cont.	4.5×3.6 @ 63°	50	···	4	5	7.8
CS(2–1)	4.5×3.6 @ 63°	1.0	3.06	25	33	7.8
CS(2–1)	4.5×3.6 @ 63°	0.125	0.38	70	95	7.8
112.4 GHz cont.	3.9×2.8 @ 70°	350	···	5	7	8.8
115.3 GHz cont.	4.3×2.8 @ −68°	88	···	10	14	7.5
CO(1–0)	4.3×2.8 @ −68°	2.0	5.20	70	95	7.5
CO(1–0)	4.3×2.8 @ −68°	0.5	1.30	145	200	7.5

[a]For the spectral line data the mean sensitivity over the entire ridge is listed for continuum-subtracted images.

Table 3. Results for 3 mm continuum emission from NGC 2024.

Source	R.A. (1950) (h m s)	Dec. (1950) (° ′ ″)	98 GHz flux density (mJy)[a]	112 GHz flux density (mJy)[a]	Spectral index, α[b]	M ($M_\odot$)
FIR2	05 39 10.85	−01 55 26.7	46±12	113±20	3.3±2.6	0.6
FIR3	05 39 11.45	−01 55 49.2	93±9	116±14	2.6±1.6	1.0
FIR4	05 39 12.49	−01 56 10.1	103±10	73±16	−0.3±2.1	0.8
FIR5	05 39 12.67	−01 57 03.3	165±10	268±16	3.6±1.4	1.7
FIR6	05 39 13.57	−01 57 27.1	145±9	175±14	1.2±1.5	1.3
FIR7	05 39 13.56	−01 57 50.2	19±12	33±20	2.1±6.9	0.2
NCP	...	...	...	...	−2.0±1.9	...
SCP	...	...	...	...	−1.3±1.5	...

[a]Integrated over a 10″ box centered on the FIR position in columns 2 and 3. Errors are statistical only. The peak at FIR7 is detected at the 2.4σ and 3.8σ level at 98 and 112 GHz respectively

[b]Value of α derived from blanked images restored with the same CLEAN beam as described in the text. The errors are 1 σ, and include calibration uncertainties of 10% at 98 GHz and 15% at 112 GHz.

Table 4. Beam-averaged brightness temperatures for the 3 mm dust emission, and lower limits to the optical depth at 350 μm assuming $\beta = 2$ and $T_d = 20$ K.

Source	$\nu = 98$ GHz		$\nu = 112$ GHz	
	T_B (K)	$\tau_{350\mu m}$	T_B (K)	$\tau_{350\mu m}$
FIR2	0.18	0.7	0.60	1.7
FIR3	0.55	2.1	0.60	1.7
FIR4	0.41	1.6	0.26	0.7
FIR5	0.91	3.5	1.56	4.5
FIR6	0.75	2.9	1.03	3.0
FIR7	0.10	0.4	0.23	0.7

REFERENCES

Anthony-Twarog, B. J. 1982, AJ, 87, 1213

Barnes, P. J., Crutcher, R. M., Bieging, J. H., Storey, J. W. V., & Willner, S. P. 1989, ApJ, 342, 883

Barnes, P. J., & Crutcher, R. M. 1990, ApJ, 351, 176

Beckwith, S. V. W., Sargent, A. I., Chini, R. S., & Güsten, R. 1990, AJ, 99, 924

Blake, G. A., Sutton, E. C., Masson, C. R., & Phillips, T. G. 1987, ApJ, 315, 621

Blake, G. A., Sandell, G., Van Dishoeck, E. F., Groesbeck, T. D., Mundy, L. G., & Aspin, C. 1995, ApJ, 441, 689

Cabrit, S., & Bertout, C. 1992, A&A, 261, 274

Chandler, C. J., Moore, T. J. T., & Emerson, J. P. 1992, MNRAS, 256, 369

Chandler, C. J., Koerner, D. W., Sargent, A. I., & Wood, D. O. S. 1995, ApJ, 449, L139

Chernin, L. M. 1996, ApJ, in press

Gaume, R. A., Johnston, K. J., & Wilson, T. L. 1992, ApJ, 388, 489

Genzel, R., & Downes, D. 1977, A&AS, 30, 145

Graf, U. U., Eckart, A., Genzel, R., Harris, A. I., Poglitsch, A., Russell, A. P. G., & Stutzki, J. 1993, ApJ, 405, 249

Hayashi, M., Ohashi, N., & Miyama, S. M. 1993, ApJ, 418, L71

Hildebrand, R. H. 1983, QJRAS, 24, 267

Ho, P. T. P., Peng, Y.-L., Torrelles, J. M., Gómez, J. F., Rodríguez, L. F., & Cantó, J. 1993, ApJ, 408, 565

Lada, E. A., DePoy, D. L., Evans, N. J., & Gatley, I. 1991, ApJ, 371, 171

Lay, O. P., Carlstrom, J. E., Hills, R. E., & Phillips, T. G. 1994, ApJ, 434, L75

Lay, O. P., Carlstrom, J. E., & Hills, R. E. 1995, ApJ, 452, L73

Lis, D. C., Carlstrom, J. E., & Phillips, T. G. 1991, ApJ, 370, 583

Mauersberger, R., Wilson, T. L., Mezger, P. G., Gaume, R., & Johnston, K. J. 1992, A&A, 256, 640

Mezger, P. G., Chini, R., Kreysa, E., Wink, J. E., & Salter, C. J. 1988, A&A, 191, 44

Mezger, P. G., Sievers, A. W., Haslam, C. G. T., Kreysa, E., Lemke, R., Mauersberger, R., & Wilson, T. L. 1992, A&A, 256, 631

Moore, T. J. T., Chandler, C. J., Gear, W. K., & Mountain, C. M. 1989, MNRAS, 237, 1P

Moore, T. J. T., & Chandler, C. J. 1989, MNRAS, 241, 19P

Moore, T. J. T., & Yamashita, T. 1995, ApJ, 440, 722

Mundy, L. G., Wootten, H. A., Wilking, B. A., Blake, G. A., & Sargent, A. I. 1992, ApJ, 385, 306

Ohashi, N., Kawabe, R., Hayashi, M., & Ishiguro, M. 1991, AJ, 102, 2054

Panagia, N., & Felli, M. 1975, A&A, 39, 1

Parker, N. D., Padman, R., & Scott, P. F. 1991, MNRAS, 252, 442

Reynolds, S. P. 1986, ApJ, 304, 713

Richer, J. S., Hills, R. E., Padman, R., & Russell, A. P. G. 1989, MNRAS, 241, 231

Richer, J. S. 1990, MNRAS, 245, 24P

Richer, J. S., Hills, R. E., & Padman, R. 1992, MNRAS, 254, 525

Sanders, D. B. & Willner, S. P. 1985, ApJ, 293, L39

Schulz, A., Güsten, R., Zylka, R., & Serabyn, E. 1991, A&A, 246, 570

Scoville, N. Z., Carlstrom, J. E., Chandler, C. J., Phillips, J. A., Scott, S. L., Tilanus, R. P. J., & Wang, Z. 1993, PASP, 105, 1482

Snell, R. L., Mundy, L. G., Goldsmith, P. F., Evans, N. J., & Erickson, N. R. 1984, ApJ, 276, 625

Subrahmanyan, R. 1992, MNRAS, 254, 719

Terebey, S., Chandler, C. J., & André, P. 1993, ApJ, 414, 759

Walker, C. K., Carlstrom, J. E., & Bieging, J. H. 1993, ApJ, 402, 655

Wilson, T. L., Mehringer, D. M., & Dickel, H. R. 1995, A&A, 303, 840

This preprint was prepared with the AAS LaTeX macros v4.0.

Figure captions

Figure 1. Continuum images of NGC 2024 obtained at 98.0 GHz (left) and 112.4 GHz (right) using the Owens Valley millimeter array. The synthesized beam for each image is listed in Table 1. Crosses denote the positions of FIR1–6 from Mezger et al. (1988), and FIR7 from Mezger et al. (1992). The contours in the 98 GHz image are at intervals of 12 mJy/beam, starting at 12 mJy/beam, and for the 112 GHz image the contours are at intervals of 15 mJy/beam starting at 15 mJy/beam.

Figure 2. The CS(2–1) emission from NGC 2024, integrated from $V_{\rm LSR}$ = 1.8 to 20.2 km s^{-1}. The continuum emission (Figure 1) has been subtracted from the data. The rms noise in the image is 0.2 Jy km s^{-1}, and the contours are at 5σ intervals of 1.0 Jy km s^{-1}. Stars mark the positions of the continuum sources identified in Table 3.

Figure 3. High-spectral resolution CS(2–1) line profiles toward the FIR5/FIR6 CS(2–1) complex. The contours denote the integrated CS(2–1) emission (Figure 2) and are spaced at intervals of 2.6 Jy km s^{-1}. The spectra are plots of flux density in Jy/beam against $V_{\rm LSR}$ in km s^{-1}.

Figure 4. First moment map of the CS(2–1) emission, obtained from the high-spectral resolution data set using a flux density cutoff of 0.5 Jy/beam in each of the 0.38 km s^{-1} channels. The greyscale runs from $V_{\rm LSR}$ = 9.5 km s^{-1} to 13.5 km s^{-1}. The bipolar outflow from FIR6 is clearly visible, as is a velocity gradient in the same sense as the outflow perpendicular to the ridge around FIR5/FIR6.

Figure 5. Contours of beam-averaged column density of hydrogen molecules, $N(\rm H_2)$, in steps of 7.4×10^{22} cm^{-2}. The thin contours represent the column density derived from the continuum emission assuming $T_{\rm d}$ = 30 K and $\beta = 1$, as described in the text. The thick contours are the column density obtained from the integrated CS(2–1) emission assuming LTE with $T_{\rm ex}$ = 40 K, and a CS abundance relative to H_2 of 2.5×10^{-9}.

Figure 6. Maps of the CO(1–0) emission in 5.2 km s^{-1} wide channels. The contours are equally spaced at intervals of 0.35 Jy/beam, starting at 0.35 Jy/beam. The LSR velocity of each panel is given at the top right in km s^{-1}. A continuum image obtained from line-free channels in the low spectral resolution CO(1–0) data has been subtracted from all the maps.

Figure 7. The outflow from FIR6 traced by CO(1–0) [left] and CS(2–1) [right], overlaid on a greyscale image of the integrated CS(2–1) emission. The position of FIR6 (Table 3) is marked by a star. In both images the blueshifted emission is given as solid contours, and the redshifted emission is given as dashed contours. The velocity ranges over which the CO(1–0) emission is integrated are −31 to 1 km s^{-1} (blueshifted) and 21 to 53 km s^{-1} (redshifted). Contours are spaced at intervals of 3.1 Jy km s^{-1}, starting at

3.1 Jy km s^{-1}. The corresponding velocity ranges for the CS(2–1) emission are 3.4 to 9.1 km s^{-1} (blueshifted) and 13.3 to 19.0 km s^{-1} (redshifted). The contours are spaced at 0.34 Jy km s^{-1}, starting at 0.34 Jy km s^{-1}.

Figure 8. The redshifted outflow from FIR4 traced by CO(1–0), overlaid on a greyscale image of the 2-μm continuum from Moore & Yamashita (1995). The position of FIR4 from Table 3 is marked as a star. The CO(1–0) emission has been integrated from 13.5 to 20 km s^{-1}, and the contours are at intervals of 2.6 Jy km s^{-1} starting at 2.6 Jy km s^{-1}.

Figure 1

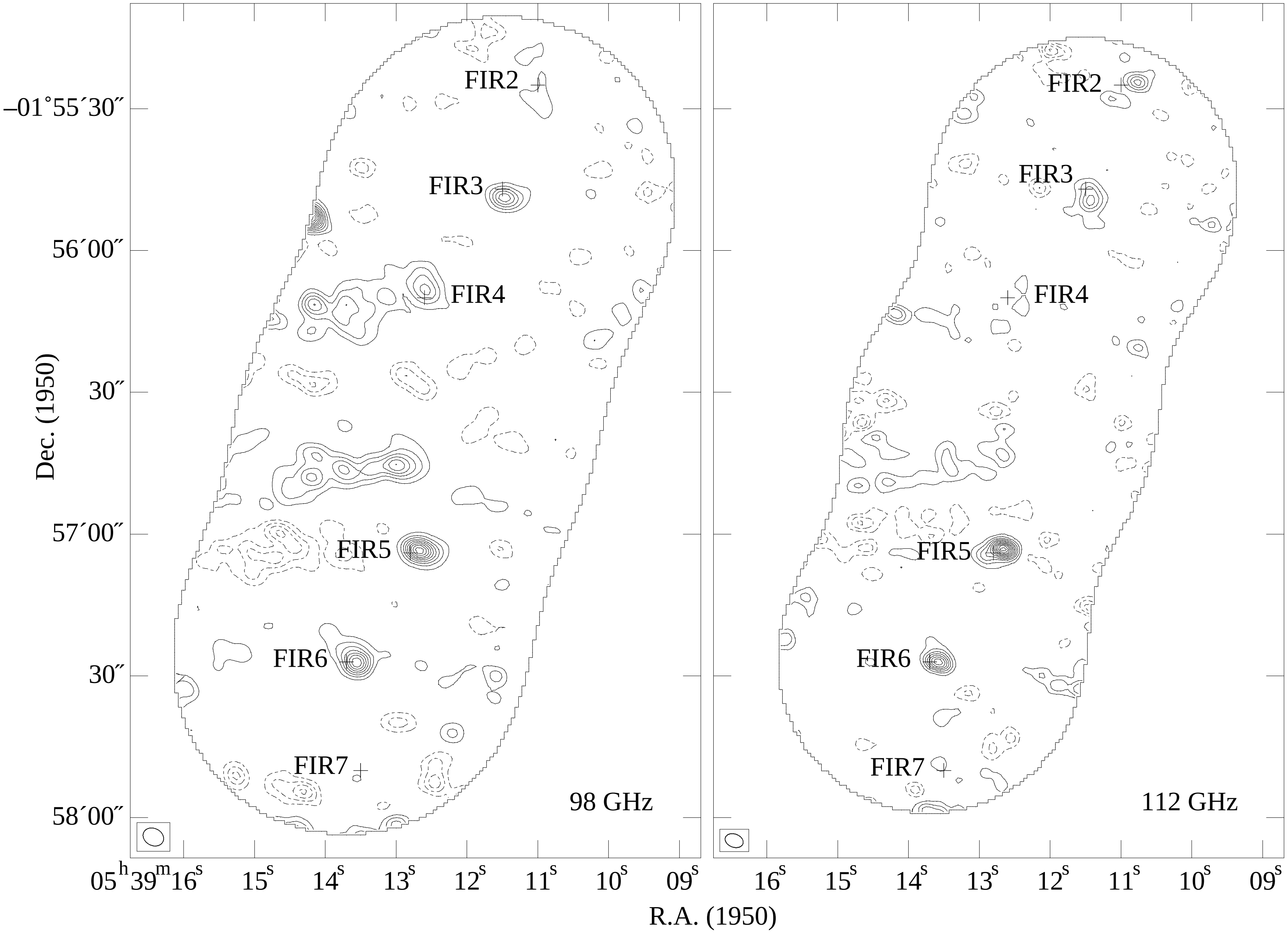
FIR2
FIR3
FIR4
FIR5
FIR6
FIR7
98 GHz
112 GHz
–01°55′30″
56′00″
30″
57′00″
30″
58′00″
Dec. (1950)
05h39m16s
15s
14s
13s
12s
11s
10s
09s
16s
R.A. (1950)

Figure 2

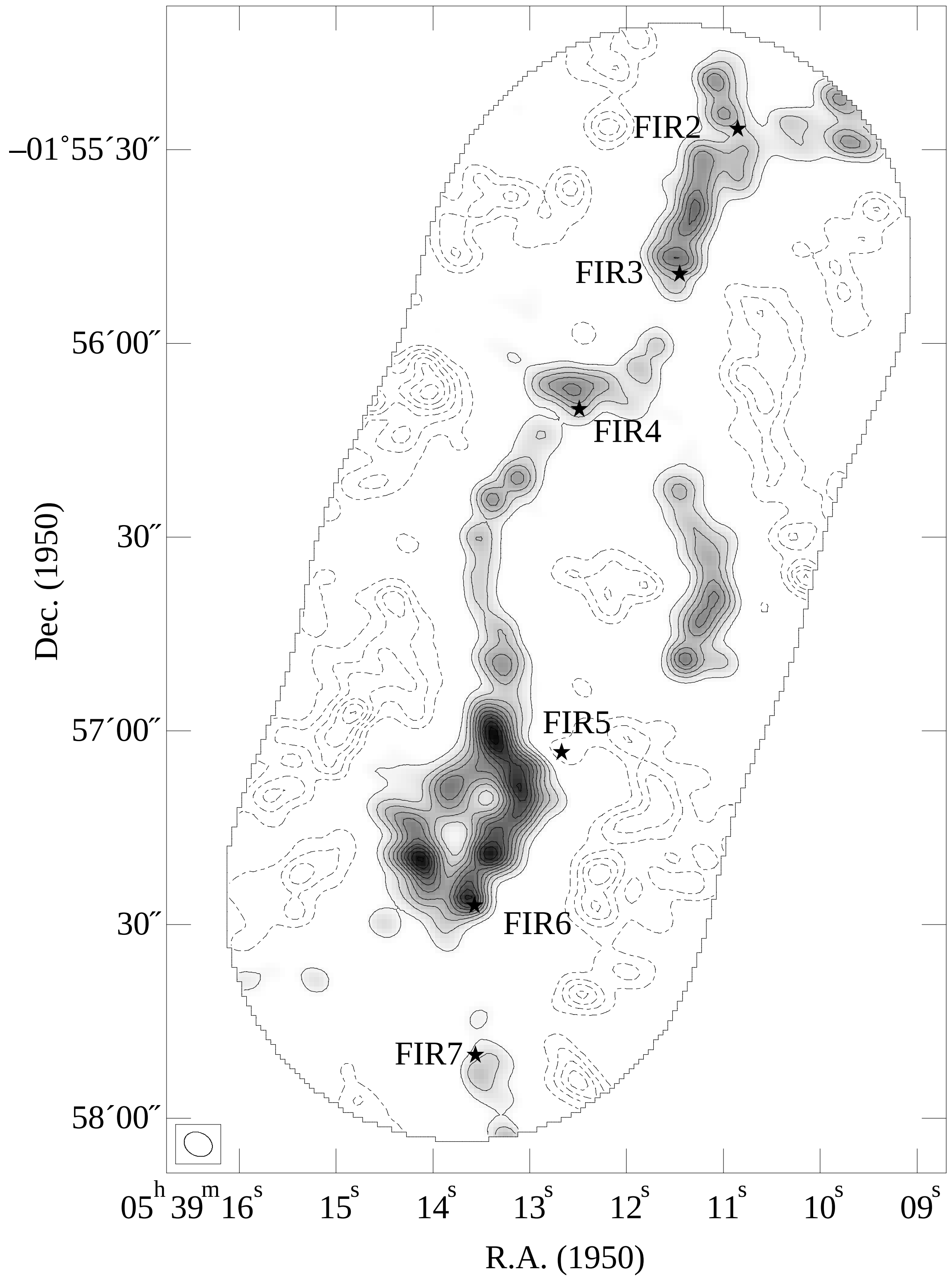
FIR2
FIR3
FIR4
FIR5
FIR6
FIR7
–01°55′30″
56′00″
30″
57′00″
30″
58′00″
Dec. (1950)
05h39m16s
15s
14s
13s
12s
11s
10s
09s
R.A. (1950)

Figure 3

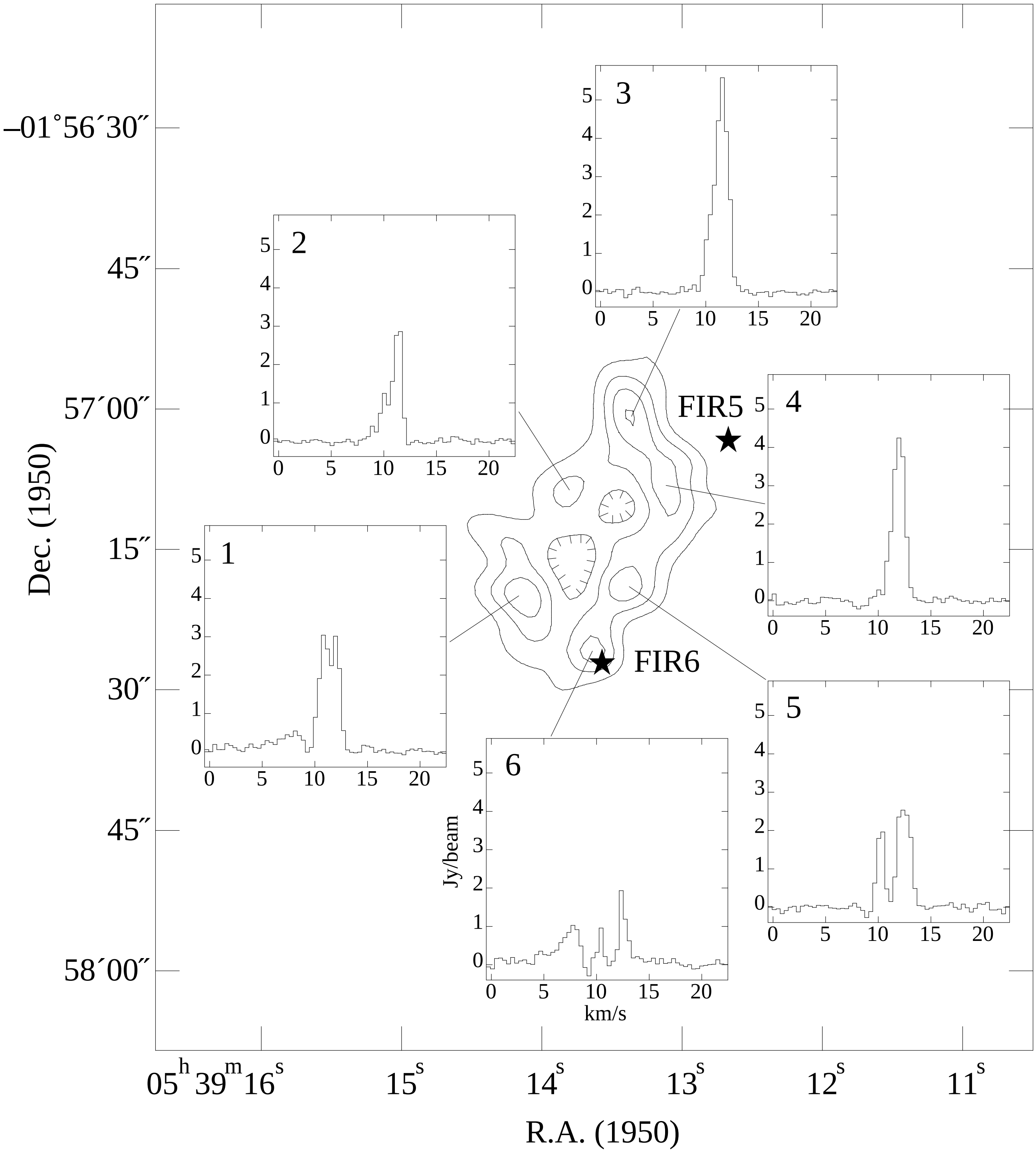

–01°56′30″
45″
57′00″
15″
30″
45″
58′00″
Dec. (1950)
05h 39m 16s
15s
14s
13s
12s
11s
R.A. (1950)
FIR5
FIR6
1
2
3
4
5
6
Jy/beam
km/s

Figure 4

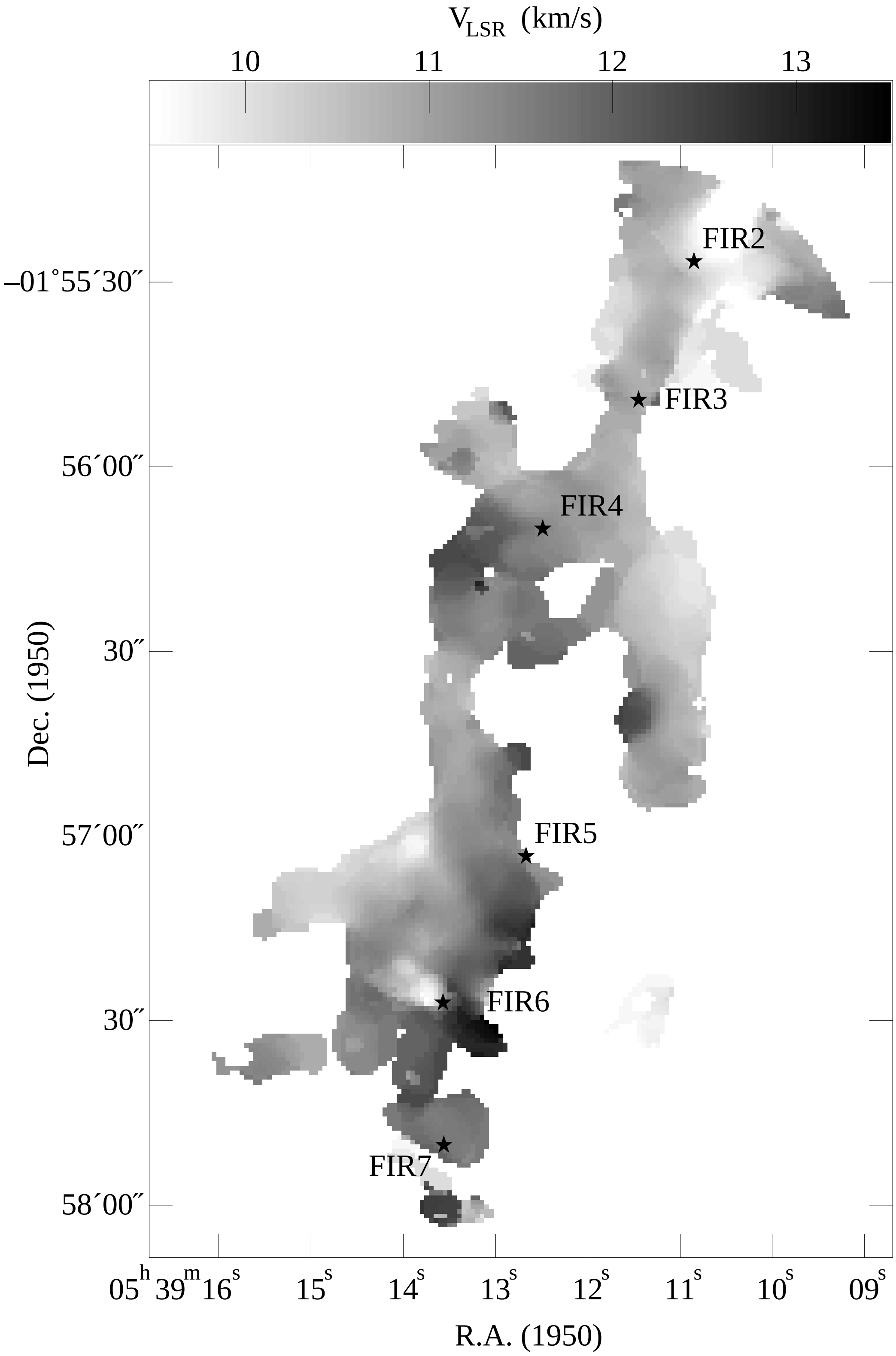
V_{LSR} (km/s)
10
11
12
13
FIR2
FIR3
FIR4
FIR5
FIR6
FIR7
–01°55′30″
56′00″
30″
57′00″
30″
58′00″
Dec. (1950)
05h 39m 16s
15s
14s
13s
12s
11s
10s
09s
R.A. (1950)

Figure 5

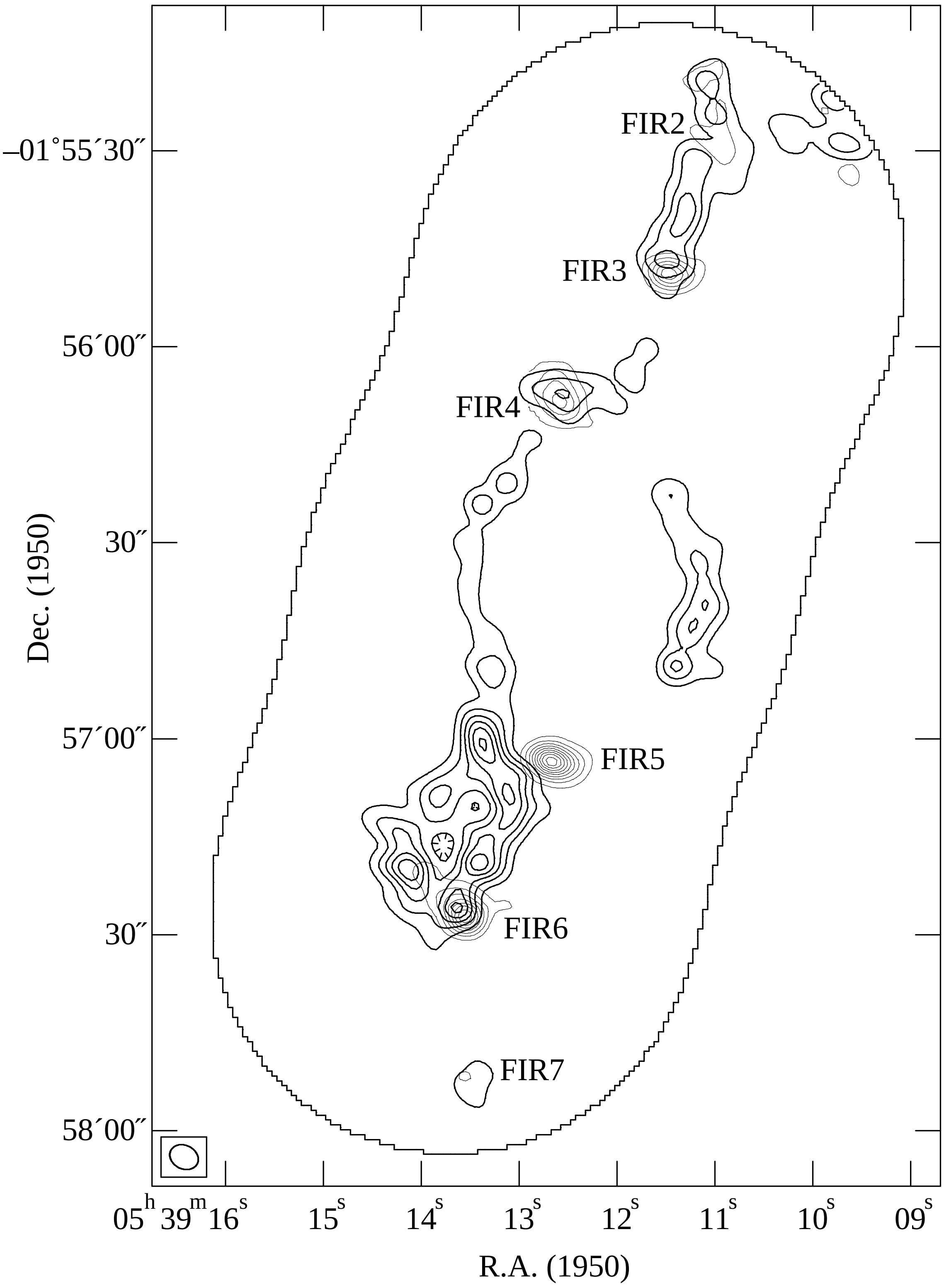
FIR2
FIR3
FIR4
FIR5
FIR6
FIR7
–01°55′30″
56′00″
30″
57′00″
30″
58′00″
Dec. (1950)
05h 39m 16s
15s
14s
13s
12s
11s
10s
09s
R.A. (1950)

Figure 6

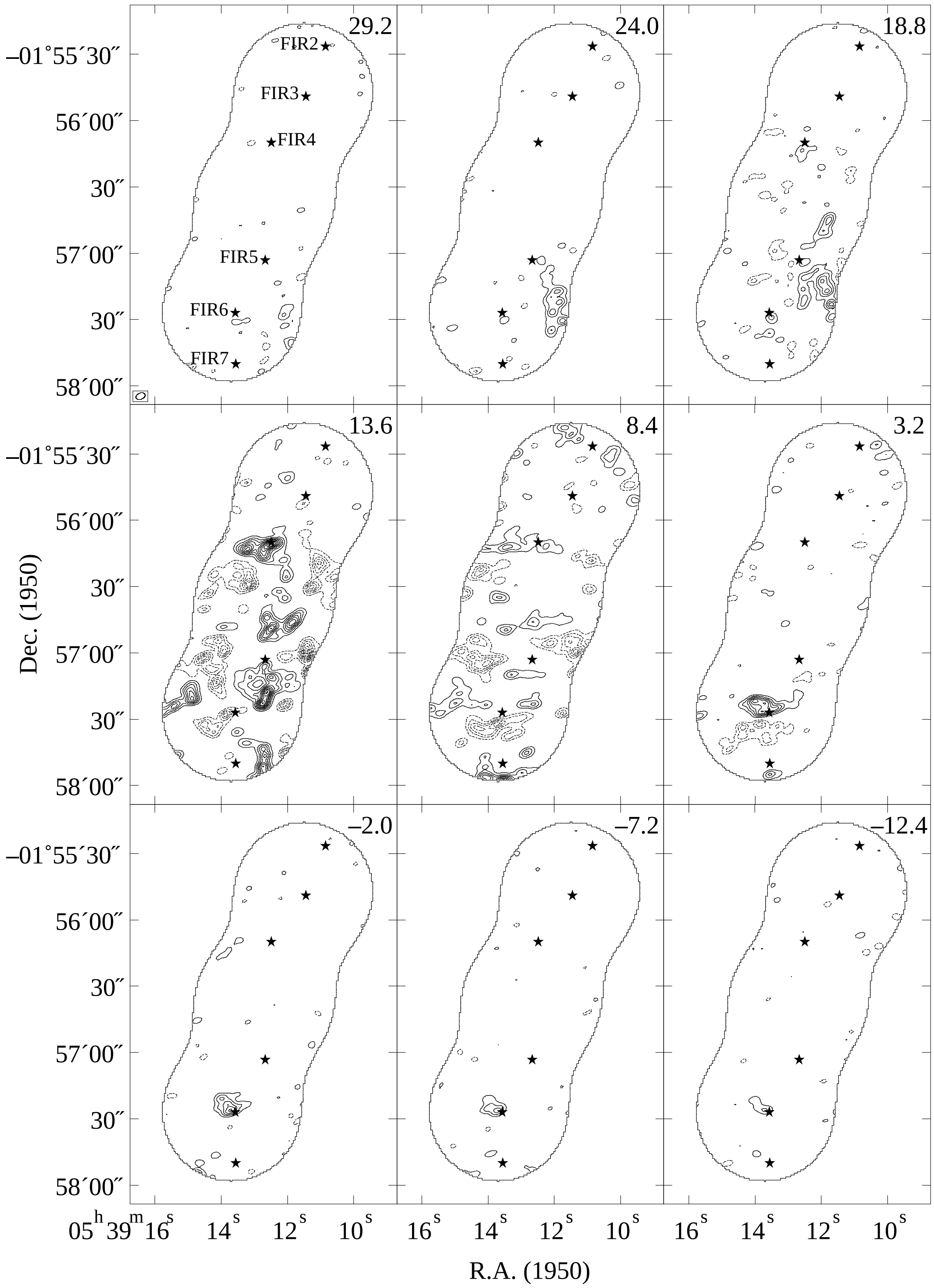
29.2
24.0
18.8
13.6
8.4
3.2
–2.0
–7.2
–12.4
FIR2
FIR3
FIR4
FIR5
FIR6
FIR7
–01°55′30″
56′00″
30″
57′00″
30″
58′00″
Dec. (1950)
05h39m16s
14s
12s
10s
16s
R.A. (1950)

Figure 7

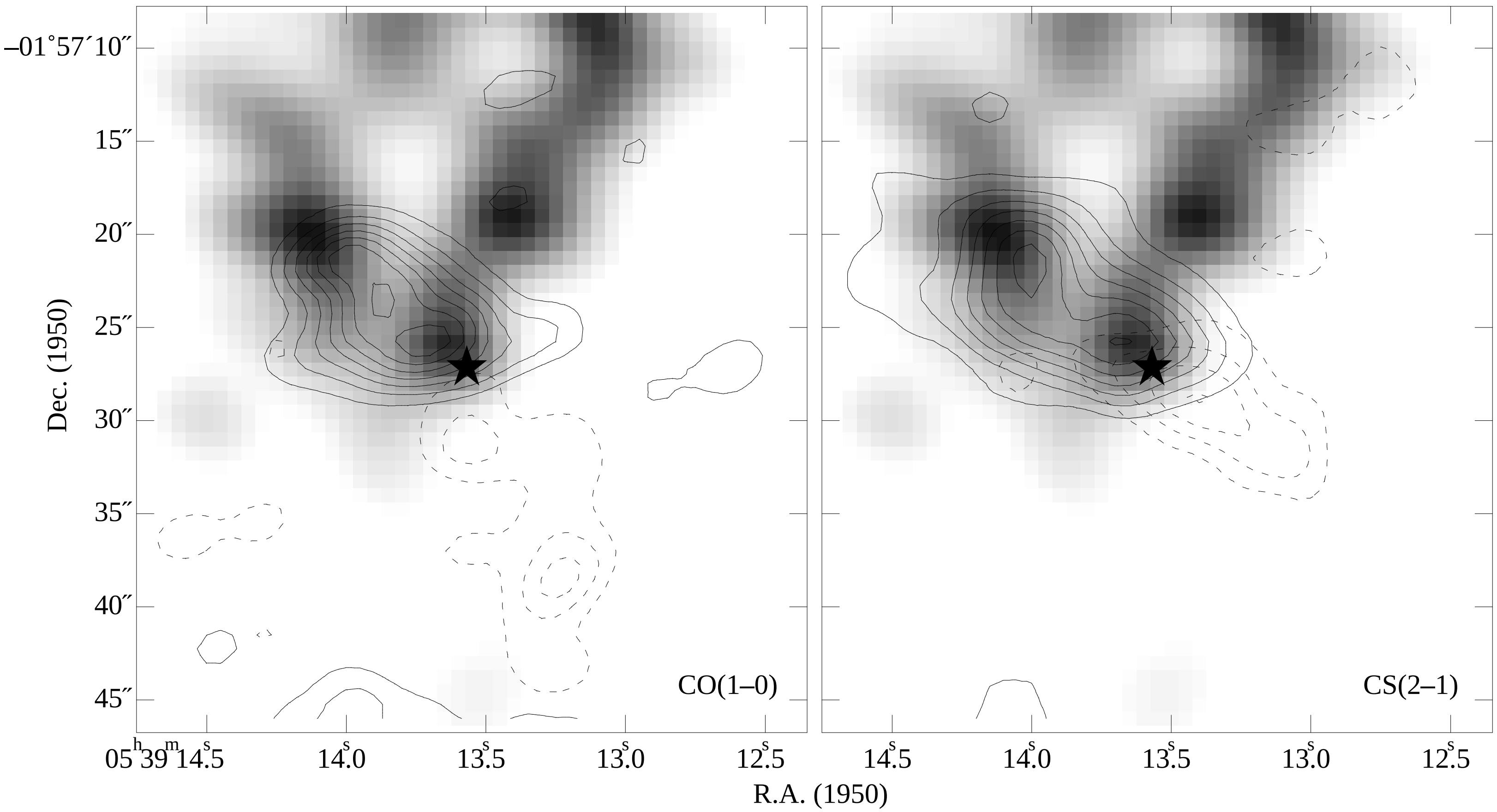

–01°57′10″
15″
20″
25″
30″
35″
40″
45″
Dec. (1950)
05h39m14.5s
14.0s
13.5s
13.0s
12.5s
14.5s
R.A. (1950)
CO(1–0)
CS(2–1)

Figure 8

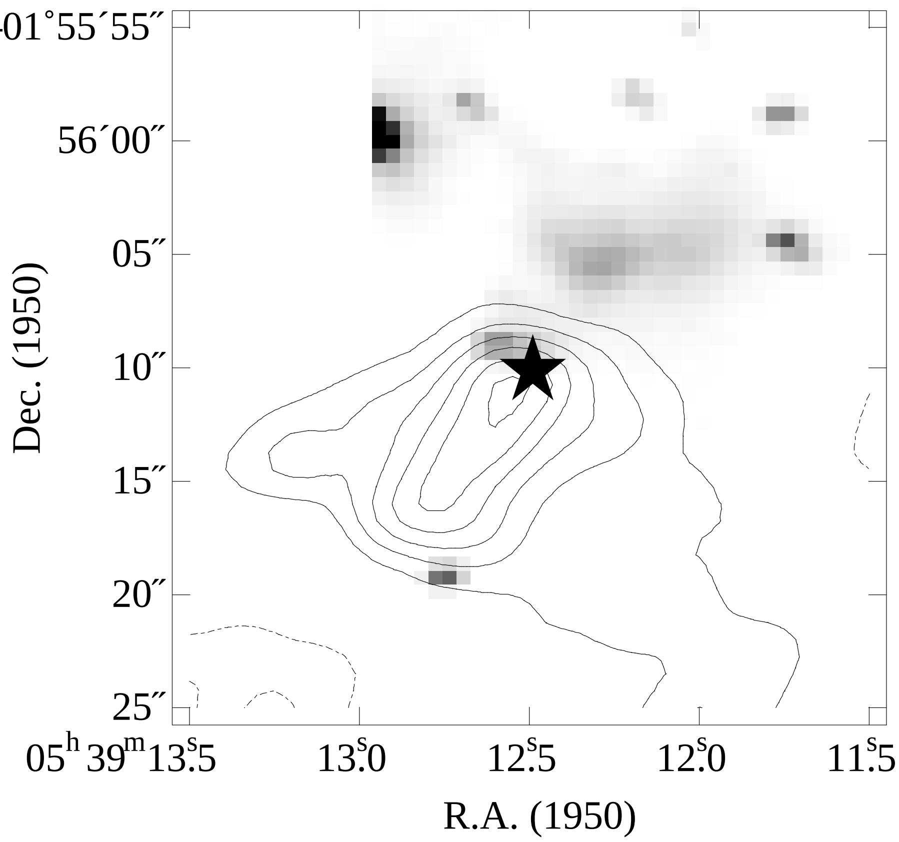
–01°55′55″
56′00″
05″
10″
15″
20″
25″
Dec. (1950)
05h 39m 13s.5
13s.0
12s.5
12s.0
11s.5
R.A. (1950)